TrapSIMD: SIMD-Aware Compiler Optimization for 2D Trapped-Ion Quantum Machines

Jixuan Ruan*
j3ruan@ucsd.edu
University of California
San Diego, USA

Hezi Zhang*
hez019@ucsd.edu
University of California
San Diego, USA

Xiang Fang
x8fang@ucsd.edu
University of California
San Diego, USA

Ang Li
ang.li@pnnl.gov
Pacific Northwest National Laboratory
Richland, USA

Wesley C. Campbell
wes@physics.ucla.edu
University of California
Los Angeles, USA

Eric Hudson
eric.hudson@ucla.edu
University of California
Los Angeles, USA

David Hayes
david.hayes@quantinuum.com
Quantinuum
Broomfield, USA

Hartmut Haeffner
hhaeffner@berkeley.edu
University of California
Berkeley, USA

Travis Humble
humblets@ornl.gov
Oak Ridge National Laboratory
Oak Ridge, USA

Jens Palsberg
palsberg@cs.ucla.edu
University of California
Los Angeles, USA

Yufei Ding
yufeiding@ucsd.edu
University of California
San Diego, USA

arXiv:2504.17886v1 [quant-ph] 24 Apr 2025

Abstract

Modular trapped-ion (TI) architectures offer a scalable quantum computing (QC) platform, with native transport behaviors that closely resemble the Single Instruction Multiple Data (SIMD) paradigm. We present FluxTrap, a SIMD-aware compiler framework that establishes a hardware–software co-design interface for TI systems. FluxTrap introduces a novel abstraction that unifies SIMD-style instructions—including segmented intra-trap shift SIMD (S3) and global junction transfer SIMD (JT-SIMD) operations—with a SIMD-enriched architectural graph, capturing key features such as transport synchronization, gate-zone locality, and topological constraints. It applies two passes–SIMD aggregation and scheduling—to coordinate grouped ion transport and gate execution within architectural constraints. On NISQ benchmarks, FluxTrap reduces execution time by up to 3.82× and improves fidelity by several orders of magnitude. It also scales to fault-tolerant workloads under diverse hardware configurations, providing feedback for future TI hardware design.

Keywords: Quantum Computing, Trapped Ion, Compilation

1 Introduction

Quantum computing (QC) has experienced rapid advancements, with multiple platforms achieving significant breakthroughs in recent years [1–9]. As each platform offers distinct advantages and continues to advance, competition among them is expected to persist. Among them, trapped ion (TI) systems, which were proposed as one of the original platforms for quantum computing around 30 years ago [10], have remained a leading candidate for quantum processors, due to the long coherence time of qubits [11] and high fidelity of various operations [12].

One of the leading trapped-ion hardware architectures is the *Quantum Charge-Coupled Device (QCCD)* model, which has become the prevailing design for scalable TI systems [11, 13–16] and has been adopted by major vendors such as Quantinuum [12, 13]. QCCD architectures feature **1D ion traps** that support fast ion transport operations, including ion shifts (moving an ion to an empty site) and ion swaps (exchanging the positions of two adjacent ions). These 1D traps are interconnected via **2D junctions**—cross-shaped structures that enable ion transport across 1D traps—thereby supporting long-range interactions and enabling modular, scalable system layouts.

Unlike superconducting platforms [17, 18] where qubits are fixed on a 2D grid and interact via static, nearest-neighbor couplings, TI systems utilize qubit transportation for program execution. This transport-based architecture enables greater flexibility, but also introduces new physical constraints that compilers must address. In particular: (1) Gate operations can only be executed when the participating qubits are not only adjacent but also co-located within a designated gate zone along the 1D trap. (2) Different operations (e.g., gates, intra-trap transports, inter-trap transports) have significantly distinct latencies [19]. (3) Inter-trap ion

transport is globally synchronized [13]: all junctions must perform the same type of transport in the same direction, which cannot conflict with intra-trap operations.

While these execution rules can be framed as hardware constraints, we view them instead as architectural features that open up new opportunities for optimization. In fact, the transport behavior of QCCD systems closely mirrors the Single Instruction Multiple Data (SIMD) paradigm in classical computing [20]. On the inter-trap level, this is reflected in the globally synchronized ion transports, where a single instruction governs uniform operations across all junctions. Within 1D traps with native single-site addressing, the SIMD perspective still offers performance benefits via grouped ion shifts (i.e., moving ions in consecutive positions toward an empty slot), which reduce routing depth and support efficient pipelining. These behaviors highlight the need for architectural abstractions and compilation optimizations that are explicitly aligned with the SIMD-style execution on TI systems.

However, existing TI quantum compilers [21, 22] are still fundamentally based on a Single Instruction Single Data (SISD) [23] execution model, which lacks the ability to express or leverage the SIMD-style behaviors inherent to QCCD architectures. For example, while these SISD compilers may occasionally produce grouped ion shift patterns, they do not actively search for or exploit them. Even if a SIMD-style grouping can be applied as a post-processing step after initial scheduling, many opportunities for grouped ion transports have already been lost due to early gate-level constraints and suboptimal routing decision. As a result, ion transport instructions often become fragmented and uncoordinated, leading to underutilized transport bandwidth.

In this work, we address two key challenges in compiler design for modular TI systems built on QCCD architectures: (1) how to develop a hardware-compatible abstraction that captures the system's transport behavior, gate zone constraints, and scheduling exclusivity, and (2) how to design compilation passes that effectively leverage the resulting design space for optimized performance.

To enable a principled hardware–software contract for QCCD systems, we first propose a novel abstraction that reflects their SIMD-style ion transport patterns (Section 3) consisting of two components: *(1) SIMD-like instruction set.* It models coordinated ion transports both within and across ion trap segments. These include a class of Segmented intra-trap Shift SIMD (S3) instructions, with each instruction dictating grouped *intra-trap* ion shifts in a specified direction, and a class of global Junction Transportation SIMD (JT-SIMD) instructions, with each instruction dictating a global *inter-trap* operation on selected ions along a specified direction. *(2) SIMD-enriched architectural graph abstraction.* It augments the traditional coupling graph by capturing TI execution constraints such as the conflict between intra-trap and inter-trap transports, position-awareness, and thermally constrained gate zones.

Despite the advantages offered by these abstractions, compile-time optimization under this framework remains highly challenging due to the expansive optimization space and potential conflicts between different SIMD instructions. To this end, we propose a novel TI compiler consisting of two key compilation passes, as shown in Figure 1. The first pass is a **SIMD Aggregation Pass** (the yellow box in Figure 1) that systematically aggregates scalar ion transport operations into wider SIMD instructions (Section 4). With a more global search than greedy approaches guided by a zone-aware cost function, it generates candidate effective SIMD instructions based on the routing needs of ions over the upcoming timesteps. The second pass is a **SIMD Scheduling Pass** (the green box in Figure 1) that selects and schedules SIMD instructions under hardware constraints (Section 5). At each timestep, it performs a hierarchical decision process that first compares all candidate JT-SIMD instructions and then compares with the cost continuing intra-trap execution, switching to the high-latency inter-trap execution until it becomes urgent or sufficient gain has accumulated. This is coordinated by a time-sliced synchronization mechanism that is aware of the latency disparity between different operations, which enables more efficient scheduling by reducing qubit idleness.

Our contributions in this paper can be summarized as below.

- We propose a novel SIMD abstraction that captures the features of modular TI architectures through a set of SIMD-style instructions and a SIMD-enriched architectural graph, along with two compilation passes tailored to TI systems.
- The SIMD aggregation pass systematically aggregates scalar ion transport operations into wider SIMD instructions via a relatively global search guided by a carefully designed heuristic cost function.
- The SIMD scheduling pass optimizes the selection and scheduling of SIMD instructions under hardware constraints through hierarchical comparison coordinated by a time-sliced synchronization mechanism.
- Through comprehensive evaluation, we show that our compiler reduces execution time by up to 3.82 × and improves fidelity by several orders of magnitude on NISQ benchmarks. For FTQC programs, we provide full support and validate its functionality across varied hardware configurations.

2 Background and Related Work

This section presents essential hardware background and summarizes existing compilation approaches for TI quantum computing.

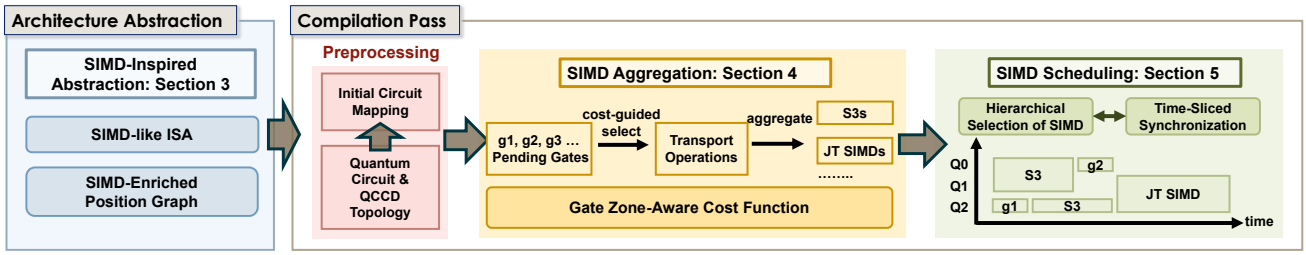

Figure 1. Overall Flow of Our Compiler

2.1 2D Trapped-Ion Hardware Architecture

This section provides key hardware background on the QCCD architecture used in modern TI quantum processors[12, 24]. The system combines 1D ion traps with 2D junctions to support scalable qubit transport, and introduces specific operational constraints that shape how programs must be compiled and scheduled.

Table 1. Fidelity and Latency Parameters of TI Operations (based on experimental data from [12, 13, 24])

operation types	operation	fidelity	latency (μs)
gate operations	1Q gate	99.9975%	5
	2Q gate	99.82%	25
	measurement	99.84%	120
transport operations	intra-trap qubit shift	99.978%	58
	intra-trap qubit swap	99.978%	200
	inter-trap qubit shift	99.956%	250
	inter-trap qubit swap	99.912%	500

1D Linear Traps. As illustrated in Figure 2(a), each linear trap consists of alternating **gate zones** (yellow) and **auxiliary zones** (gray), following a layout widely adopted in Quantinuum's architecture [24]. Gate zones support high-fidelity quantum operations, while auxiliary zones serve as storage locations without gate functionality. The number and placement of gate zones are constrained not only by hardware resources, but also by thermal and optical limitations, as densely packed operations can increase heat dissipation and calibration complexity[25]. Therefore, each zone typically holds at most one ion to minimize crosstalk [12].

Gate Operations. Within a trap, **gate instructions** include single-qubit (1Q) and two-qubit (2Q) operations, executed via laser pulses [24] in gate zones. Notably, a 2Q gate only acts on ions co-located in the same gate zone, requiring ions to be shifted in and out for interaction, as shown in Figure 2(a). This implicit transport is accounted for in the gate's effective latency. As summarized in Table 1, 2Q gates generally contribute the most to the overall error due to the complexity of entangling operations, though they remain fast when applied in well-calibrated zones.

Intra-Trap Transport. In addition to gate execution, intra-trap transport operations allow repositioning of ions within a trap via two mechanisms: *intra-trap shift*, which moves ions through adjacent empty zones, and *intra-trap swap*, which exchanges positions with a neighboring ion. As shown in Figure 2(a) and detailed in Table 1, intra-trap shifts are typically faster and more reliable than intra-trap swaps. However, both forms of transport are more latency-intensive than gate execution and should be coalesced or minimized when possible for efficiency.

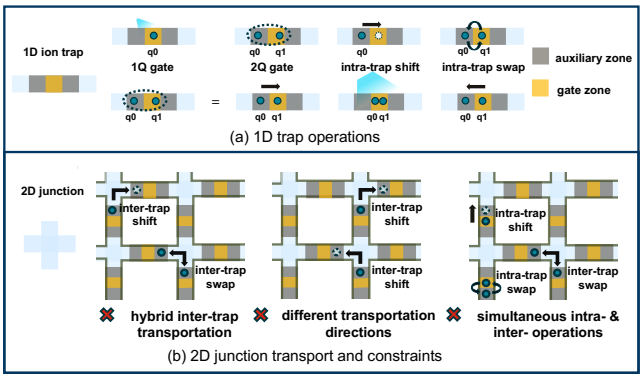

Figure 2. Trapped-Ion Transport and Operation Model

2D Junction. To enable scalable quantum transport beyond isolated 1D traps, modern TI architectures incorporate 2D junctions [13, 15, 26], which interconnect linear segments to form a 2D QCCD-style grid [12]. Each 2D junction connects up to four trap segments at orthogonal angles, supporting bidirectional transport in horizontal and vertical directions. By utilizing such junction-connected segments, the architecture enables modular and dense layout expansion while avoiding long 1D chains. This facilitates reduced transport distances [13], increases gate-zone density, and supports more parallel computation.

Inter-Trap Transport. Inter-trap transport is achieved through two global operations: *(1) inter-trap shift*, where ions move from edge zones into empty positions of neighboring traps (Figure 2(b)), and *(2) on-site inter-trap swap*, where adjacent edge ions exchange positions (Figure 2(b)). These operations are globally synchronized: at each cycle, a single transport type (shift or swap) and direction (e.g., left-to-bottom) is selected and broadcast system-wide on all the participating ions at the 2D junctions. Compared to intra-trap transport,

these inter-trap operations are slower and more error-prone due to longer physical trajectories and increased susceptibility to decoherence, as shown in Table 1.

In summary, there are three key constraints imposed on inter-trap transport: (1) only one type of operation (shift or swap) may be issued per cycle; (2) all transport must occur in the same global direction; and (3) intra-trap and inter-trap transport cannot proceed simultaneously due to distinct control pathways, as illustrated in Figure 2(b). These constraints places new demands on the software stack, requiring specialized scheduling strategies to coordinate transport efficiently.

2.2 Previous Compilation Strategies for TIQC

Many existing approaches [21, 22] borrow abstractions or heuristics from superconducting systems [27] and apply them to TI hardware, incorporating some TI-specific constraints but still overlooking key aspects of QCCD architecture. For instance, although each intra-trap transport is lower in cost and more flexible than inter-trap transport, the cumulative volume of intra-trap transport can still be substantial and must be scheduled carefully. Nonetheless, prior compilation strategies have typically overlooked the cost of intra-trap transport, focusing solely on inter-trap routing. They have also abstracted away globally synchronized junction usage and sparsely distributed gate zones and instead used simple models that miss major optimization opportunities.

Despite these limitations, prior work introduces useful abstractions and scheduling heuristics for inter-trap routing. We adopt two representative strategies as baselines in our evaluation and adapt them to reflect realistic hardware constraints. One direction, exemplified by **SHAPER** [21], builds on the SABRE compiler—originally developed for superconducting qubits—by modeling ion positions as nodes in a position graph and applying SABRE's swap-based scheduling. While SHAPER focuses primarily on inter-trap routing, we extend its SABRE-based approach to also handle intra-trap transport using a similar swap-to-shift reinterpretation strategy. In contrast, **QCCDsim** [22] adopts a custom heuristic tailored to trapped-ion inter-trap transport optimizations. It precomputes inter-trap transport paths and performs congestion-aware gate scheduling. We reuse both SHAPER and QCCDsim's mapping and scheduling outputs and augment them with an additional scheduling pass that enforces hardware constraints, including mutual exclusivity between intra- and inter-trap operations and conflict resolution among inter-trap transports with different directions.

3 SIMD-Inspired Abstractions for Ion Transport

In this section, we propose a novel abstraction that reflects the SIMD-style ion transport patterns of TI machines. Our abstraction includes: (1) a set of SIMD-like instructions and (2) a SIMD-enriched architectural graph abstraction. This abstraction forms the foundation for the compiler optimizations presented in Section 4 and Section 5.

3.1 SIMD-like ISA

To enable modular control scheduling and systematic optimization over ion transport, we define a hardware-aligned abstraction layer composed of two SIMD-like instruction classes. These instruction classes serve as ISA-style transport primitives that reflect the physical execution constraints and layout granularity of QCCD architectures (Figure 3):

1. Segmented Intra-trap Shift SIMD (S3): We define *Segmented Shift SIMD (S3)* as an instruction class that models grouped intra-trap ion shifts. With each linear trap segment acting as a virtual SIMD lane, one or more groups of ions can perform concurrent shifts along various directions. We abstract each grouped shift as an S3 instruction, which specifies: (i) a direction (left or right), and (ii) the ions to shift in this group. The number of ions moved by each S3 instruction is referred to as its *data width*. For example, Figure 3(a) illustrates 3 configurations of grouped ion shifts within a 10-ion segment: three S3 instructions of data width 3, two S3 instructions of data width 4 and one S3 instruction of data width 9. This instruction class enables compilers to express grouped transport patterns directly, improving intra-trap transport efficiency by aligning software logic with hardware-native execution capabilities.

2. Global Junction Transfer SIMD (JT-SIMD): We define *Junction Transfer SIMD (JT-SIMD)* as an instruction class that models globally synchronized inter-trap ion transports. Each JT-SIMD instruction encodes a system-wide transport mode across all 2D junctions in a QCCD grid, which specifies: (i) a transport type (shift or swap), (ii) a global transport direction (e.g., left-to-right, top-to-left) and (iii) the junctions that participate the transport (each individual junction may choose to participate or remain idle). According to (i) and (ii), JT-SIMD instructions are categorized into 18 subclasses—12 for directional shifts and 6 for directional swaps—each corresponding to a legal routing path through the X-junctions (Figure 3(b)). At each timestep, only one JT-SIMD instruction can be issued, reflecting the hardware-level constraint of global synchronization. This instruction class enables the compiler to reason about long-range transport with explicit awareness of global coordination requirements.

3.2 SIMD-Enriched Position Graph

Our instruction-level abstractions are paired with a refined architectural graph model that extends previous *position graph* models for TI architectures [21]. In a position graph, nodes represent physical locations in the 1D traps, rather than logical qubits as in coupling graphs widely used in superconducting systems [28]. This reflects the dynamic ion occupancy in TI systems and naturally distinguishes *shift*

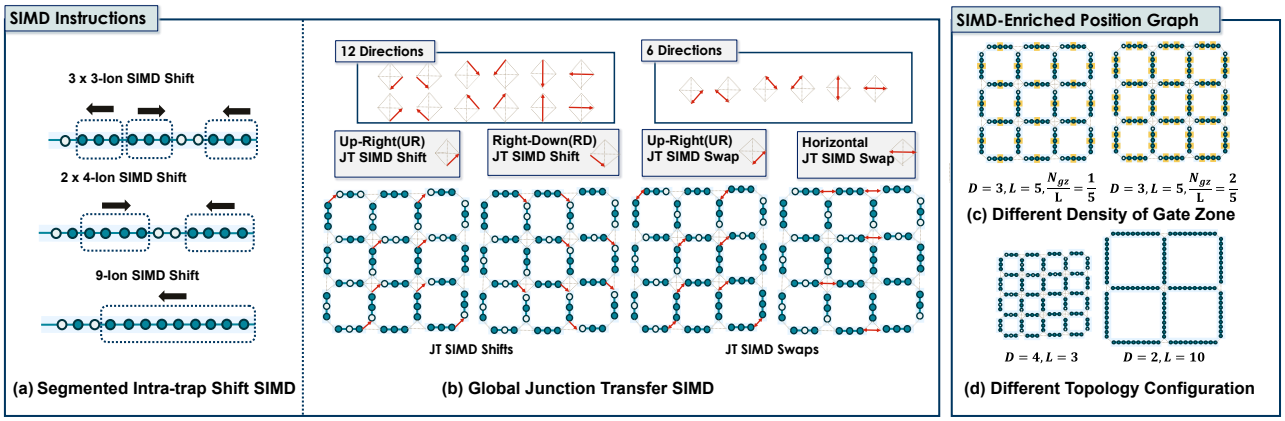

Figure 3. Overview of SIMD Architecture

(into empty sites) from *swap* (between occupied sites) operations. While this model is useful, it remains incomplete in capturing full hardware semantics. Here, we introduce three key extensions to build a SIMD-enriched coupling graph abstraction.

1. Dynamic Switchable Position Graph: The conflict between different JT-SIMD instructions and that between JT-SIMD and intra-trap operations require a dynamic notion of connectivity. Rather than using a static position graph, we define a *switchable position graph* that changes dynamically with the active instructions. At any given time step, the position graph switches between an intra-trap mode which only consists of intra-trap couplings and an inter-trap mode which only consists of inter-trap couplings in a specified direction. This dynamic coupling model is similar to reconfigurable interconnect fabrics in classical architectures and more accurately reflects the time-varying transport capabilities of QCCD systems. It avoids inefficient routing by ensuring a natural compliance with the hardware constraints.

2. Gate Zone integrated Position Graph: In traditional coupling graphs for superconducting devices, each node represents a qubit and each edge indicates the ability to apply a two-qubit gate between connected qubits. However, in ion-trap systems, these capabilities are decoupled. While ions may move along an edge in a position graph, gate operations can only occur within designated *gate zones*. This distinction is yet missed in previous abstraction [21]. Figure 3(c) illustrates different gate zone placements in various densities. In large-scale hardware, gate zones are typically placed sparsely along linear trap segments to reduce control, calibration and thermal overhead [25, 29]. Our abstraction explicitly encodes gate zone locations within the position graph, ensuring the compiler's awareness of these dedicated locations. More importantly, it enables a feedback loop between software and hardware: software-level scheduling can alleviate gate zone congestion, and hardware teams can adapt gate zone layout based on compiler-informed guidance—a co-design opportunity not captured by previous abstractions.

3. Configurable Trap and Junction Topology: Beyond logical constraints, our abstraction enables software visibility into key physical design choices—specifically, the tradeoff between extending linear trap segments versus increasing the number of 2D junctions. As illustrated in Figure 3(d), multiple architectures may host the same number of ions using different topological configurations: longer intra-trap segments with fewer junctions, or more frequent junctions with shorter trap segments. These decisions influence hardware complexity, control parallelism, and thermal scalability. By exposing these design axes explicitly, our abstraction allows software and compiler strategies to target hardware-specific tradeoffs, enabling layout-sensitive scheduling, and traffic-aware routing.

4 SIMD Aggregation Pass

With SIMD-style instructions and architectural abstractions defined, the compiler must generate execution plans that expose parallelism, respect hardware constraints, and reduce routing cost. The first step is to aggregate scalar ion transports into SIMD-style instructions by analyzing spatial patterns and upcoming gate demands. This section presents how intra-trap S3 and inter-trap JT-SIMD operations are formed using a gate-zone-aware cost function.

4.1 Instruction Aggregation Strategies

1. Intra-Trap S3 Aggregation: To maximize intra-trap transport efficiency, our approach proactively constructs shift sequences that leverage position reuse—each selected shift frees its source position for subsequent moves. The process begins by scanning pending gates to identify qubits whose movement in a particular direction would reduce their heuristic cost. For example, in Figure 4, both Q3 and Q4 intend to shift into the same empty position, leading to

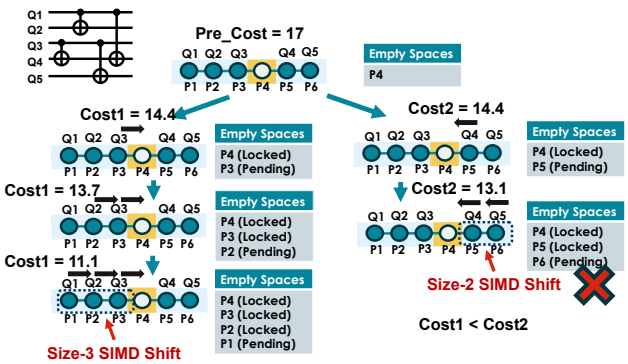

Figure 4. SIMD-Aware S3 Formation with Position Reuse

a potential conflict. Rather than resolving this greedily, we initiate a timeline-aware forward search to explore viable shift sequences. Starting with Q3, we trace a path where Q2 and Q1 can shift ahead of it in the same direction. As each shift is selected, we lock the destination position to prevent further contention and release the source position to allow follow-up shifts. This forms a candidate group shift Q1, Q2, Q3. A similar process applied to Q4 reveals another candidate group shift Q4, Q5. In general, this process produces multiple group shifts across the 1D trap. Some groups are independent—they operate in different regions and do not compete for the same empty space—and can thus be scheduled in parallel. Others, like Q1, Q2, Q3 and Q4, Q5, conflict due to shared dependencies, and must be evaluated against one another. We use our gate zone-aware heuristic to compare the total benefit of each conflicting group, and choose the one that provides the greatest forward progress. In this case, Q1, Q2, Q3 achieves a lower heuristic cost and is selected for execution.

2. Inter-Trap JT-SIMD Aggregation: We examine inter-segment routing requirements and generate instructions from the 18 predefined JT-SIMD classes. For each possible global transport (e.g., down shift, upright shift), we evaluate qubits involved in upcoming two-qubit gates and determine whether shifting or remaining stationary yields a lower heuristic cost. The ions selected for transport under each operation are then aggregated into a single JT-SIMD instruction. For example, in the case of a global down shift, we compare the cost of shifting each qubit downward versus keeping it in place, and aggregate those benefiting from downward movement into a unified instruction.

4.2 Gate Zone-Aware Cost Function

To effectively guide SIMD aggregation and transport scheduling, our compiler employs a gate zone-aware heuristic that integrates both spatial and temporal priorities. This heuristic prioritizes gates whose qubits are positioned favorably with respect to their assigned gate zones and penalizes those with higher routing overhead. Specifically, it evaluates each gate in the front layer based on (1) the cumulative distance from participating qubits to the target gate zone, $d_{\text{gz}}(g)$, and (2) the relative distance between qubits for two-qubit gates, $d_{\text{inter}}(g)$, to discourage zone congestion, as shown in Figure 5. The second term is weighted by a coefficient α and included only when the gate is a two-qubit operation. This selective inclusion is controlled by the indicator $\mathbb{I}_{\text{tg}}(g)$, which is set to 1 only for two-qubit gates. We set $\alpha = 0.3$ in our implementation to reflect that inter-qubit distance is not the dominant factor during placement and routing. This ensures that the compiler prioritizes minimizing gate zone distance while still incorporating spacing when congestion arises. To reduce search overhead, each pending gate is assigned a target zone only once during compilation. Reassignment of gate zones is triggered only under excessive routing delays, preserving scalability. To further mitigate congestion, gates targeting overloaded zones are deprioritized, and in cases of persistent congestion, our scheduler may temporarily ignore some gates that require future transport assistance when computing the heuristic cost. Formally, the heuristic cost is given by:

$$C(\mathcal{G}, \pi) \quad = \sum_{g \in F,\ g.\text{qubits} \notin E} \left(d_{\text{gz}}(g) + \alpha \cdot \mathbb{I}_{\text{tg}}(g) \cdot d_{\text{inter}}(g) \right) \tag{1}$$

Here, G denotes the SIMD-enriched position graph that encodes zone-level connectivity and constraints, and π is the current mapping from logical qubits to physical positions. F denotes the set of ready gates in the dependency graph (the front layer), and E is the set of qubits currently involved in in-flight operations. Unlike traditional compilers—which overlook gate zone availability and rely on sparse ion placement to avoid contention—our heuristic enables high-density layouts and efficient gate scheduling by dynamically co-optimizing qubit transport and gate placement. It integrates trap-level congestion and transport-induced scheduling delays into a unified cost model, serving as a simulator-driven feedback loop during compilation.

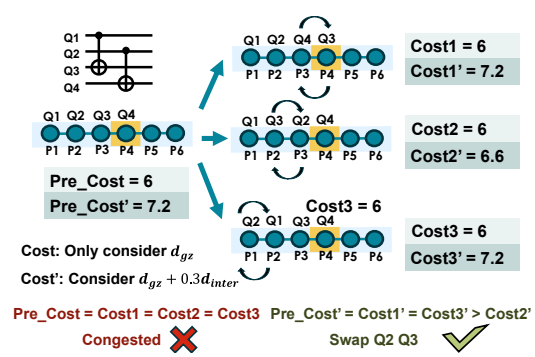

Figure 5. Alleviating Gate Zone Congestion via Spacing-Aware Prioritization

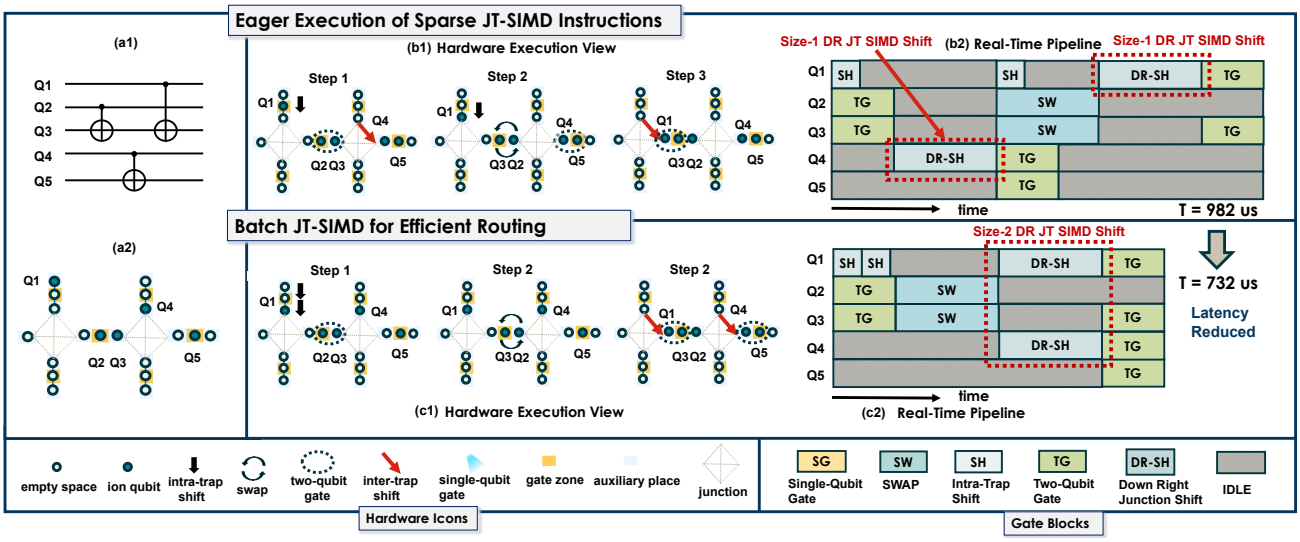

Figure 6. Better SIMD Scheduling via Optimized Intra–Inter Transport Switching: This example illustrates the benefit of our compiler's decision rule, which activates JT-SIMD instructions only when their routing gain exceeds that of intra-trap alternatives, enabling more effective batching. The circuit and its initial layout are shown in (a1) and (a2). (b1) and (b2) depict the baseline scheduler, which greedily triggers inter-trap movements, resulting in fragmented transport. In contrast, our optimized scheduler in (c1) and (c2) delays and aggregates JT-SIMD instructions to align transport directions, improving SIMD efficiency and reducing overhead.

5 SIMD Scheduling Pass

To efficiently execute aggregated SIMD instructions, the compiler must schedule them under hardware constraints such as control exclusivity and thermal limits [25], which stem from limited laser power and gate zone heating. This section introduces a two-stage scheduling strategy: (1) a hierarchical decision process that selects the best JT-SIMD instruction and determines whether to continue intra-trap or switch to inter-trap transport, and (2) a time-sliced synchronization mechanism that coordinates execution at a fine-grained level to improve latency management and throughput. Together, these techniques enhance gate readiness while reducing contention and routing delays.

5.1 Hierarchical Selection of SIMD Instructions

This subsection outlines a hierarchical scheduling strategy that governs which SIMD instruction types to issue at each timestep. It first selects the optimal JT-SIMD class based on projected layout improvement, then dynamically decides between intra-trap and inter-trap instructions by balancing latency, thermal cost, and global routing benefit.

1. Selection of JT-SIMD Class per Cycle: At each clock cycle, only one JT-SIMD class is allowed. Our scheduler calculates the heuristic score of the 18 pre-defined JT-SIMD instructions, with a lookahead into operations over the next few timesteps. Then it schedules the one with the lowest cost, enabling the most progress in terms of ready-to-route ions.

2. Intra-Trap versus Inter-Trap Prioritization: In trapped-ion systems, intra-trap and inter-trap SIMD instructions cannot be executed simultaneously due to hardware-level control restrictions. Moreover, inter-trap transport operations typically incur 2–3× higher latency and larger thermal overhead compared to intra-trap shifts. To effectively coordinate these transport types, our scheduler dynamically selects between intra-trap S3 and inter-trap JT-SIMD instructions by comparing their potential to reduce the overall heuristic cost. At each scheduling step, the compiler evaluates two candidate transport plans: one composed purely of intra-trap S3 shifts, and another that includes inter-trap JT-SIMD instructions. The scheduler prioritizes intra-trap S3 instructions for their lower latency and less thermal overhead, while activating inter-trap JT-SIMD opportunistically to unlock critical inter-trap routing progress. Specifically, global inter-trap transport is initiated only when its benefit to routing significantly outweighs that of intra-trap alternatives. Let $C(G, \pi)$, as mentioned in Section 4, denote the current heuristic cost of the system layout, and let π_{intra} and π_{inter} represent the resulting qubit mappings after applying intra-trap and inter-trap transports, respectively. The condition of selecting inter-trap JT-SIMD can be expressed as:

$$C(G, \pi) - C(G, \pi_{\text{inter}}) > 2 \cdot (C(G, \pi) - C(G, \pi_{\text{intra}})) \quad (2)$$

This decision rule naturally enables the aggregation of more inter-trap transports, thereby enhancing the transport efficiency. Fig. 6 demonstrates this benefit with an example of

implementing the circuit in Fig. 6(a1) with an initial layout in Fig. 6(a2). A traditional compiler has no decision rule like Rule (2) and would eagerly execute JT-SIMD instructions once their cost is lower than S3 instructions. This would lead to an operation scheduling with the steps shown in Fig. 6(b1). **Step 1:** the 2Q gate between Q2 and Q3 is first conducted as these two qubits are adjacent. Meanwhile, Q1 and Q3 can be brought closer by an intra-trap down shift on Q1, while Q4 and Q5 can be brought closer by an inter-down-right shift on Q4. Due to hardware constraints, the latter one is scheduled after the former one is complete, as shown in Fig. 6(b2). **Step 2:** The 2Q gate between Q4 and Q5 is conducted since the two qubits are adjacent now. Concurrently, Q1 and Q3 are brought further closer by further shifting down Q1 and swapping Q2 and Q3. **Step 3:** An inter-trap shift on Q1 is conducted to bring Q1 adjacent to Q3, so that the 2Q gate between Q1 and Q3 can be conducted now. Taking the latency of each operation into account, this scheduling can be translated to that in Fig. 6(b2), leading to an overall computation time of 982μs. Note that while the two inter-trap shifts are in the same direction, they are conducted separately due to the eager execution of JT-SIMD instructions.

In contrast, with the decision rule above, our compiler can provide an optimized scheduling that identifies and groups inter-trap transports along the same direction. With the same example, our compiler would schedule operations in the following steps, as represented by Fig. 6(c1). **Step 1:** The 2Q gate between Q2 and Q3 is first conducted as these qubits are adjacent. Concurrently, Q1 is shifted down for two steps to get closer to Q3. **Step 2:** Q2 and Q3 are swapped to bring Q3 closer to Q1. **Step 3:** Q1 and Q4 are shifted in the down-right direction by a global inter-trap transportation to bring them adjacent to Q3 and Q5, so that the two 2Q gates between Q1,Q3 and between Q4,Q5 can be conducted. The primary optimization in these steps is that our compiler delays and groups the inter-trap shifts on Q1 and Q4 to reduce transportation latency. As shown in Fig. 6(c2), this reduces the overall computation time to 732μs only.

5.2 Time-sliced SIMD Synchronization

In a scheduling process, operations may complete at different times due to their distinct latencies, effectively dividing execution into fine-grained time slices. To improve scheduling within each time slice, we propose a synchronization mechanism that enhances scheduling precision and minimizes qubit idle time by tracking real-time execution information.

This mechanism handles three types of information at each time slice: (1) qubit usage — it tracks which qubits are engaged in operations and which are idle, preventing the scheduling of operations that require the currently engaged qubits; (2) position availability — it monitors which positions are occupied or free, enabling immediate scheduling of operations once space is freed by other operations; and (3) program dependencies — it maintains a dynamic dependency graph for the program to identify executable operations as soon as their prerequisites complete.

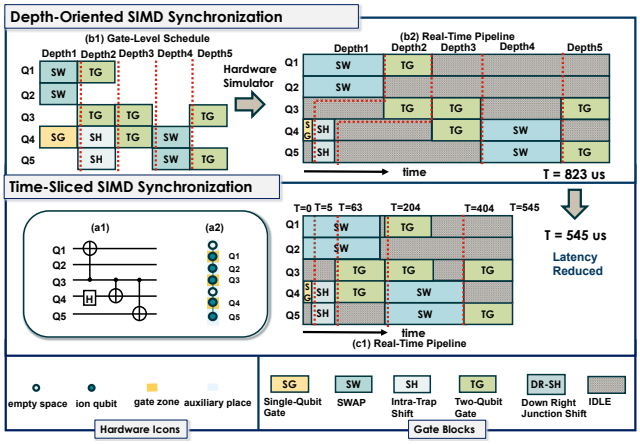

Figure 7. Improved Execution via Time-Sliced SIMD Synchronization: This example demonstrates how our fine-grained scheduler overlaps operations by leveraging real-time context. (a1) and (a2) show the circuit and initial layout. The baseline plan (b1, b2) follows depth-based scheduling and leaves idle gaps.

To determine how time advances within the scheduling cycle, we adopt different strategies depending on the type of chosen transport. For intra-trap transport, we use the shortest remaining time (SRT) approach, where the scheduler advances time by the duration of the operation that finishes earliest. This allows the system to quickly release qubits and space resources, enabling other operations to proceed without unnecessary delay. In contrast, when inter-trap transport is scheduled, the system switches to a longest remaining time (LRT) strategy, waiting for all in-flight intra-trap operations to complete before initiating any inter-trap transport. This avoids execution conflicts due to hardware constraints and allows inter-trap operations to be executed in a clean, batched manner.

Together, these mechanisms provide the scheduler with up-to-date execution context and enable precise control over transport execution, improving both temporal utilization and overall circuit efficiency. The advantage of our fine-grained synchronization can be illustrated by an example in Fig. 7, where the TI systems implements the circuit in Fig. 7(a1) with an initial layout in Fig. 7(a2). A traditional compiler has no awareness of latency disparity and would employ depth-oriented synchronization, with operations scheduled in the steps shown in Fig. 7(b1). In the traditional strategy (Fig.7(b1)), the compiler assumes all operations in the same step complete simultaneously, thus missing opportunities for overlap. **Step 1:** The 1Q gate is conducted on Q4. Concurrently, Q1 and Q3 are brought adjacent by swapping Q1 with Q2. **Step 2:** With the 1Q gate and the Q1–Q2 swap presumed

completed, the compiler proceeds to schedule the 2Q gate between Q1 and Q3. At the same time, Q4 and Q5 are shifted upward in preparation for subsequent gates with Q3. **Step 3:** The 2Q gate between Q3 and Q4 is conducted. **Step 4:** Q5 is brought adjacent to Q3 by swapping with Q4. **Step 5:** The 2Q gate between Q3 and Q5 is conducted. Taking the latency of each operation into account, this scheduling can be translated to that in Fig. 7(b2), leading to an overall computation time of $823\mu s$.

In contrast, with the time-sliced synchronization, our compiler can produce a better scheduling as shown in Figure 7(c1), which has the following steps. **Step 1:** The 1Q gate is conducted on Q4, while Q1 and Q3 are brought adjacent by swapping Q1 with Q2. **Step 2:** Notably, our compiler detects that the 1Q gate on Q4 has already finished while the swap is still ongoing, and immediately schedules a grouped S3 shift on Q4 and Q5 to move them toward Q3—an opportunity missed by depth-based synchronization. **Step 3:** The 2Q gate between Q3 and Q4 is conducted, considering that the swap gate between Q1 and Q2 is still executing. **Step 4:** After the 2Q gate between Q3 and Q4 is completed, we then swap Q4 and Q5 to bring Q4 adjacent to Q3, and conduct the 2Q gate between Q1 and Q3. **Step 5:** This is followed by the 2Q gate between Q3 and Q5.

The main difference between our scheduling and the depth-oriented scheduling is that we fill up the time of the swap operation between Q1 and Q2 with the execution of 2Q gate between Q3 and Q4. We remark that this cannot be identified by compilers with a depth-oriented synchronization, despite that the 2Q gate between Q1 and Q3 and that between Q3 and Q4 are actually commutable. This is because as shown in 7(b1), they would think that the shift on Q4 has to be initiated after the completion of swap between Q1 and Q2, hence the 2Q gate cannot between Q3 and Q4 are not executable until the next depth. This forces the compiler to choose the 2Q gate between Q1 and Q3 in the current depth. Overall, our time-sliced synchronization leads to a shorter computation latency of $545\mu s$.

6 Evaluation

This section evaluates our SIMD-aware compiler and demonstrates its effectiveness in reducing execution time and improving fidelity by leveraging SIMD-style transport in both intra- and inter-trap operations. This evaluation also provides practical insights for future hardware design, especially under varying architectural constraints and connectivity trade-offs.

6.1 Experiment Setup

Baselines. We compare our compiler against two representative baselines adapted to the QCCD architecture: SHAPER* and QCCD-SIM. SHAPER* is adapted from state-of-the-art SHAPER strategy [21], originally developed for all-to-all connected architectures including superconducting and ion-trap systems. We reconstruct a baseline by combining its position graph abstraction with SABRE-style heuristics, tailored to our trapped-ion hardware constraints. QCCD-SIM [22] shares SHAPER's idealized connectivity model but uses a simpler inter-trap scheduling strategy. It lacks a general scheduling framework and does not support intra-trap transport, so we evaluate its inter-trap transport component only, combined with our intra-trap solution. For fair comparison. we strengthen each baseline with a SIMD-style post pass that groups aligned transports in their scheduling into SIMD instructions, enabling parallelism absent in their native frameworks. Further details on both baselines and their adaptations can be found in Section 2.

Table 2. NISQ Benchmark Programs.

#Qubits	DxD (Grid Shape)	Grid Layout	Number of 1D Trap	N_{gz} (Number of Gate Zones / Trap)	L (1D Trap Capacity)
20	2x2		12	2	8
					14
40	3x3	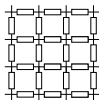	24	2	8
					14
60	4x4	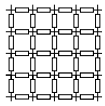	40	2	8
					14
100	5x5	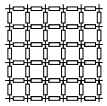	60	2	8
					14

Benchmarks. We evaluate performance using a diverse suite of benchmarks under both NISQ and FTQC settings.
(1) *NISQ Applications.* We select a variety of benchmark programs, including Quantum Approximate Optimization Algorithm (QAOA), Ripple-Carry Adder (RCA) [30], Bernstein-Vazirani (BV), and Variational Quantum Eigensolver (VQE), across multiple circuit sizes, as summarized in Table 2. QAOA is implemented on randomly generated 3-regular graphs, where ZZ gates are applied only between graph-connected qubits. BV circuits are generated using random secret strings with balanced distributions of 0s and 1s. For VQE, we employ a standard full-entanglement ansatz, known for its expressive power [31, 32].
(2) *FTQC Applications.* To evaluate FluxTrap in the fault-tolerant regime, we use QFT-20 and QSim-20 [33, 34] circuits protected by surface codes, exploring code distances ranging

from 3 to 11. This selection ensures realistic program success probabilities while maintaining hardware resource demands within the scope of expected advancements over the next 5–10 years (physical error rate: 0.1%–0.01%, total qubit count: 1,000–20,000) [35, 36].

Metrics. We evaluate our compiler's performance using different metrics tailored to the NISQ and FTQC settings described above:

(1) *NISQ Applications.* In comparisons with *SHAPER**, we consider two primary metrics: *Execution Time* (T_{exe}), which includes the total duration of 1Q and 2Q gates as well as intra-/inter-trap shift and swap operations; and *Fidelity (F)*, modeled as $F = F_{1Q} \cdot F_{2Q} \cdot F_{\text{transport}} \cdot F_{decoh}$ [12, 37], where $F_{1Q} = f_{1Q}^{N_{1Q}}$, $F_{2Q} = f_{2Q}^{N_{2Q}}$, $F_{\text{transport}} = f_{\text{intra_shift}}^{N_{\text{intra_shift}}} \cdot f_{\text{intra_swap}}^{N_{\text{intra_swap}}} \cdot f_{\text{inter_shift}}^{N_{\text{inter_shift}}} \cdot f_{\text{inter_swap}}^{N_{\text{inter_swap}}}$, and $F_{\text{decoh}} = exp(-n\ T_{exe}\ /\ T_{coh})$ with n denoting the number of qubits in the program. Here, N terms denote the respective operation counts, while each fidelity term reflects the accumulated degradation from specific gate or transport operations. We set the coherence time $T_{coh} = 600s$ based on reported values from state-of-the-art TI hardware [38]. Additionally, when comparing inter-trap scheduling performance against QCCDsim and SHAPER*, we report inter-trap transport schedules as a separate metric to account for differences in hardware instruction latency.

(2) *FTQC Applications.* For fault-tolerant workloads, we focus on *Execution Time* (T_{exe}) as the primary metric, since we can suppress the logical error rate by increasing the code distance [35], as we show in Figure 10(a).

Hardware setting. For an n-qubit benchmark, the hardware layout is shown in Table 2. Given that Quantinuum's 1D ion trap hardware can accommodate a maximum of around 20 ion qubits [12], we selected trap sizes of 8 and 14 qubits. Each trap has 2 gate zones for two-qubit gates. We chose this layout with more vacant space because the maximum program size that SHAPER* can schedule is limited by the number of gate zones. Performance in more compact layouts will be discussed further in Figure 11.

Evaluation Methodology. This subsection details the evaluation methodology for the two experimental settings.

(1) *NISQ Applications.* FluxTrap computes program execution time with the discrete event scheduler described in Section 5, based on instruction durations listed in Table 1. To model fidelity, we compute the overall circuit fidelity using the total execution time and operation counts, i.e., N_{1Q}, N_{2Q}, $N_{\text{intra_shift}}$, $N_{\text{intra_swap}}$, $N_{\text{inter_shift}}$, and $N_{\text{inter_swap}}$, alongside their respective instruction fidelities, also listed in Table 1.

(2) *FTQC Applications.* In the fault-tolerant setting, operations are performed on entire surface-code logical qubits. Programs are decomposed to Clifford+T gate set [39], with logical CNOT and H gates executed transversally and logical T gates implemented via gate teleportation [39–41]. Unlike NISQ operations, the scheduling of T gates must also coordinate the transport of data qubits toward pre-generated magic states, introducing additional spatial and temporal complexity. We adopt the surface-code layout mapping strategy from [42], which maps each logical patch onto a grid of traps, with one physical qubit—either data or syndrome—assigned per trap to facilitate parallel control and scalable scheduling in QCCD architectures. To estimate logical error rates, we use `Stim` simulator [43] under the TI noise profile shown in Table 1 and Pymatching for decoding and error correction [44]. In our experiments, we focus on the execution time of logical operations and omit syndrome extraction time, as it is roughly proportional to the logical gate latency [35].

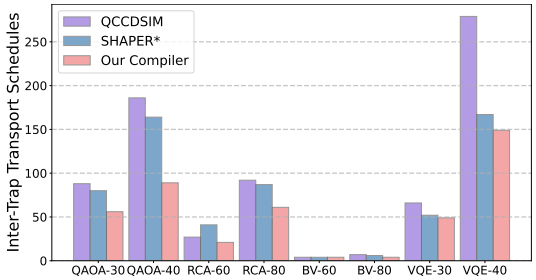

Figure 8. Comparison of Inter-Trap Transport Performance

6.2 Results for NISQ Applications

We first compare FluxTrap with SHAPER* under two 1D trap capacities ($N_{trap} = 8$ and $N_{trap} = 14$), focusing on execution time (T_{exe}) and fidelity. To better understand the source of improvements, we break down T_{exe} into intra- and inter-trap transport times, and fidelity into transport, decoherence and two-qubit gate fidelity. Secondly, We compare with QCCDsim focusing on inter-trap transport performance, as its routing strategy does not support intra-trap transport evaluation (Section 2).

Overall Performance. Table 3 shows that FluxTrap significantly outperforms SHAPER* in both execution time and fidelity. For $L = 8$, we observe up to a **3.04**× reduction in execution time and multi-order-of-magnitude improvements in fidelity across benchmarks of varying sizes. At $L = 14$, these improvements grow further—reaching up to **3.82**× in execution time and even greater gains in fidelity. These results underscore the scalability and efficiency of our compiler, enabled by its SIMD-aware design that promotes coordinated routing and execution via aggregated transport.

Ablation Analysis. We further compare the breakdown of time and fidelity components with SHAPER* on a 5×5 layout with 1D trap capacity of 3 and one computation zone per trap. We adopt this constrained configuration to amplify the scheduling challenges and better highlight the benefits of our SIMD-aware transport and coordination strategies. The

Table 3. Results of our compiler and SHAPER*. Each 'benchmark-n' corresponds to an n-qubit circuit in the circuit model.

L (1D Trap Capacity)	Benchmark - #Qubit	SHAPER* $T_{exe}(\mu s)$	Our $T_{exe}(\mu s)$	$T_{exe}(\mu s)$ Improv.	SHAPER* Fidelity	Our Fidelity	Fidelity Improv.
8	QAOA-20	173,561	93,845	1.85	0.49	0.61	1.25
	RCA-20	214,369	70,624	3.04	0.43	0.57	1.32
	BV-20	9,870	8,373	1.18	0.97	0.97	1.0
	VQE-20	218,974	130,538	1.68	0.42	0.56	1.33
	QAOA-40	733,637	327,601	2.24	0.03	0.13	4.21
	RCA-40	487,001	180,950	2.69	0.16	0.28	1.78
	BV-40	21,554	16,175	1.33	0.92	0.94	1.02
	VQE-40	883,977	532,440	1.66	0.02	0.09	4.66
	QAOA-60	1,684,718	744,943	2.26	2.93×10^{-04}	8.91×10^{-03}	30.36
	RCA-60	801,437	278,970	2.87	0.05	0.14	2.82
	BV-60	37,866	23,625	1.6	0.88	0.92	1.05
	VQE-60	1,921,069	1,255,877	1.53	8.54×10^{-05}	3.33×10^{-03}	39.04
	QAOA-100	4,687,884	2,256,313	2.08	3.56×10^{-11}	5.85×10^{-07}	1.64×10^{4}
	RCA-100	1,346,070	561,586	2.4	5.25×10^{-03}	0.03	5.65
	BV-100	66,858	38,679	1.73	0.74	0.86	1.16
	VQE-100	5,200,261	3,570,854	1.46	8.33×10^{-13}	8.88×10^{-08}	1.07×10^{5}
14	QAOA-20	265,068	128,886	2.06	0.38	0.58	1.53
	RCA-20	303,805	85,702	3.54	0.35	0.56	1.63
	BV-20	13,233	11,745	1.13	0.96	0.97	1.01
	VQE-20	300,942	134,186	2.24	0.3	0.55	1.86
	QAOA-40	1,053,797	370,858	2.84	8.02×10^{-03}	0.12	15.23
	RCA-40	689,769	204,547	3.37	0.1	0.27	2.76
	BV-40	31,426	18,479	1.7	0.9	0.94	1.05
	VQE-40	1,223,741	784,346	1.56	3.07×10^{-03}	0.07	21.41
	QAOA-60	2,403,532	822,641	2.92	1.25×10^{-05}	8.01×10^{-03}	639.78
	RCA-60	1,131,689	296,592	3.82	0.02	0.14	6.74
	BV-60	50,583	28,741	1.76	0.81	0.91	1.13
	VQE-60	2,669,385	1,551,403	1.72	1.05×10^{-06}	2.48×10^{-03}	2357.99
	QAOA-100	6,450,674	2,568,088	2.51	1.19×10^{-15}	3.51×10^{-07}	2.94×10^{8}
	RCA-100	1,900,434	572,560	3.32	1.06×10^{-03}	0.03	29.59
	BV-100	106,961	60,293	1.77	0.66	0.83	1.27
	VQE-100	7,226,433	4,329,181	1.67	1.20×10^{-18}	9.58×10^{-09}	8.00×10^{9}

ablation study helps isolate the benefits introduced by our SIMD-aware instruction set and scheduling strategy.

(1) *Time Ablation.* Figure 9(a1)–(d1) break down intra- and inter-trap execution times, with our results shown in red and SHAPER* in blue. In each plot, the solid line represents inter-trap transport time, while the lighter line denotes intra-trap transport. Although inter-trap transport generally dominates total latency due to its higher per-operation cost, intra-trap movement remains non-negligible, especially in interaction-heavy circuits. Our compiler consistently reduces both components, with particularly notable improvements in QAOA and VQE benchmarks that involve more remote interactions, as shown in Figure 9(a1)(d1). These gains stem from our SIMD-aware design: S3 instructions accelerate intra-trap shifts via parallel execution, while JT-SIMD batching reduces synchronization overhead for inter-trap transport. This is further enhanced by our gate zone-aware heuristic, which aligns qubit transport and aggregation patterns with zone availability to minimize routing cost. The advantages become more pronounced with increasing qubit count, highlighting the scalability of our approach.

(2) *Fidelity Ablation.* Figure 9(a2)–(d2) shows a fidelity breakdown comparing SHAPER* (blue/light blue) and FluxTrap (red/-light red), with the common two-qubit gate fidelity plotted as a purple reference line. Intuitively, the overall transport fidelity should outperform that of two-qubit gates, as each transport operation has significantly higher fidelity than two-qubit gates. However, under inefficient scheduling strategies such as SHAPER*, excessive ion transport can degrade overall transport fidelity, pushing it below that of two-qubit gates (solid blue in Figure 9(a1)–(d1)). Additionally, prolonged execution time exacerbates decoherence errors (light red in Figure 9(a1)–(d1)). In contrast, our SIMD-aware, hardware-compatible compiler minimizes redundant movements and shortens execution duration, preserving transport fidelity above the two-qubit gate baseline and keeping decoherence errors low—particularly in complex benchmarks like QAOA and VQE, as shown in Figure 9(a2)–(d2).

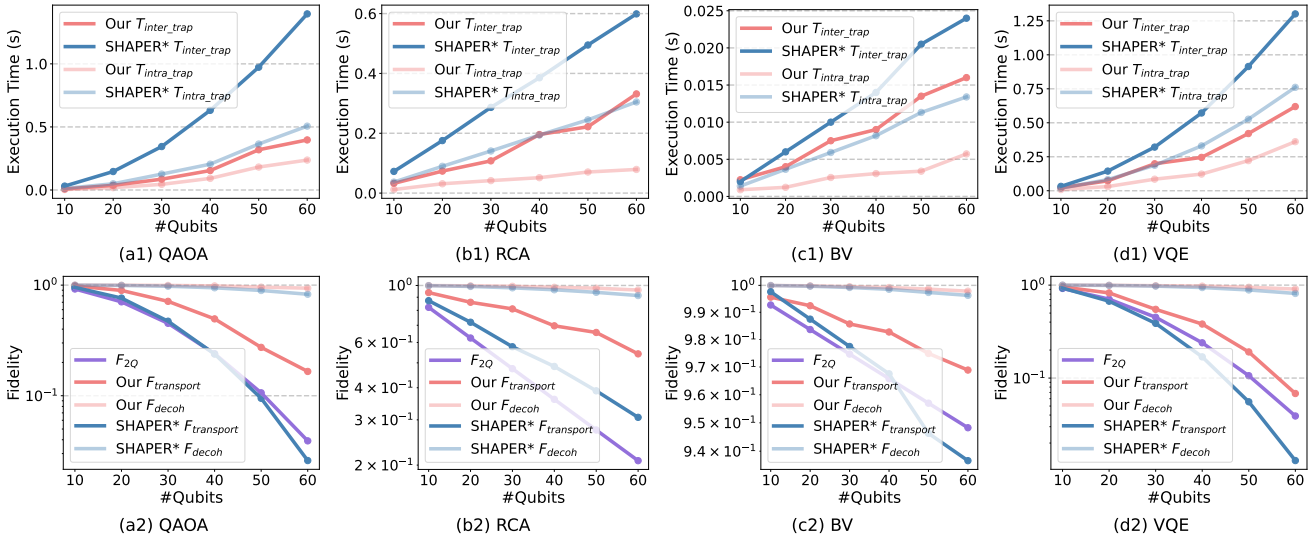

Figure 9. (a1)–(d1) show execution time breakdowns for QAOA, RCA, BV, and VQE, highlighting intra- vs. inter-trap transport. (a2)–(d2) show fidelity breakdowns into two-qubit gate, transport (shift/swap) errors and decoherence errors.

Inter-trap Scheduling Comparison with QCCDsim. As shown in Figure 8, SHAPER* (blue) generally outperforms QCCDsim (purple) due to its more refined heuristic score analysis for routing steps. Notably, FluxTrap (red) achieves better performance than both, as it enhances routing with our SIMD-aware JT-SIMD transport model, which enables coordinated inter-trap transport and reduces synchronization overhead. On average, our approach delivers a 1.55× improvement over QCCDsim and a 1.42× improvement over SHAPER*. As the program size and routing complexity increase, the advantages of our method become more pronounced, particularly in benchmarks QAOA and VQE.

6.3 Results for FTQC Applications

In this subsection, we present the results of extending our compiler to FTQC, with a focus on surface codes. First, we evaluate the LER for surface codes with varying distances under the physical error profile in Table 1. As shown in Figure 10(a), a surface code with a distance of 11 achieves a logical error rate of 10^{-8}, which meets the LER requirement of our benchmarks. Next, we analyze the impact of gate zone density on execution time for surface codes with distances of 3, 7, and 11, using the QFT-20 and QSIM-20 benchmarks. As shown in Figures 10(b) and (c), a moderate number of zones can effectively reduce execution time, making a large number of gate zones unnecessary for realizing FTQC.

6.4 Implications for TI Hardware Design

To better understand how our SIMD-aware compiler adapts to different hardware settings, we conduct a sensitivity analysis under varying computation zone densities and hardware topologies, while keeping the total number of qubits fixed.

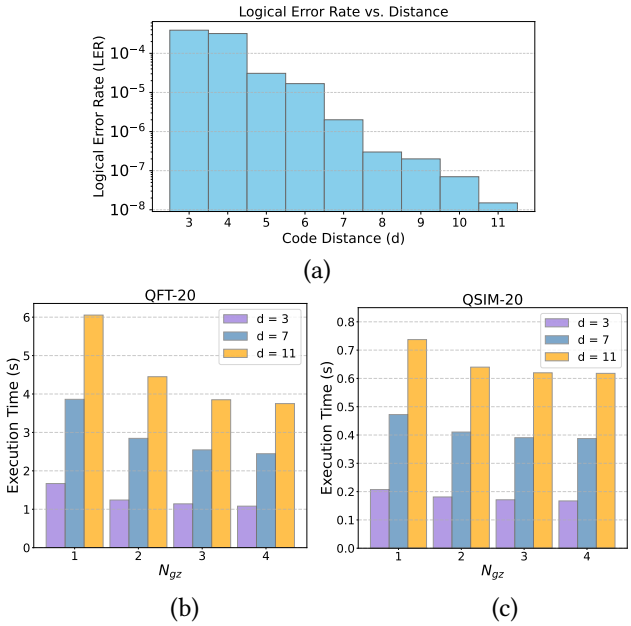

Figure 10. Evaluating Fault-Tolerant Execution: Logical Error Rates and Execution Time of QFT-20 and QSIM-20 under Varying Gate Zone Counts

Beyond demonstrating the flexibility of our approach, these experiments provide actionable insights into how hardware parameters—such as gate zone layout and trap granularity—affect system-level performance. These results reflect not only the benefits of SIMD-driven scheduling but also the effectiveness of our gate-zone-aware compilation strategy, offering practical guidance for co-designing future trapped-ion architectures.

Gate Zone Density. We evaluate the impact of gate zone density on execution time using a 3×3 grid, where each 1D trap has a capacity of 14. As shown in Figure 11(a), execution time decreases as gate zone density increases, with improvements becoming marginal beyond 20–30%, especially in the VQE benchmark. This suggests that over-provisioning computation zones brings limited returns. The optimal density is workload-dependent, and thus this result highlights an important hardware insight: gate zone allocation should be tuned based on program gate density rather than maximized blindly.

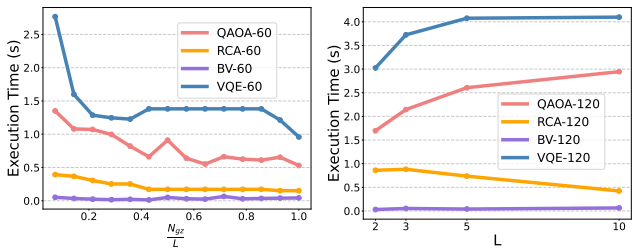

(a) (b)

Figure 11. Sensitivity analysis under varying hardware parameters. N_{gz} denotes the number of gate zones per 1D trap; L denotes the 1D trap capacity.

Impact of Hardware Topology Connectivity. We further explore how grid connectivity influences performance by varying 1D trap capacities under a fixed hardware budget of 120 qubits. Benchmarks are run on 5×5, 4×4, 3×3, and 2×2 grids corresponding to trap capacities of 2, 3, 5, and 10. As shown in Figure 11(b), benchmarks requiring highly non-local connectivity (e.g., QAOA and VQE) benefit from denser grid structures, which provide more flexible connectivity for routing. In contrast, RCA—with less frequent non-local interactions—performs better in sparser grids. These findings suggest that hardware designers should balance trap capacity and spatial density according to the expected workload class, rather than pursuing a one-size-fits-all design.

7 Conclusion

We present FluxTrap, a SIMD-aware compiler framework for modular trapped-ion quantum machines. By aligning compiler logic with the native transport behavior of QCCD architectures, FluxTrap enables efficient coordination of ion movement and gate execution. Its design combines a hardware-native SIMD abstraction with a scalable scheduling strategy, significantly improving execution time and fidelity. Evaluations across both NISQ and FTQC benchmarks confirm its effectiveness under realistic hardware constraints. As trapped-ion systems scale toward tile-based architectures and memory-like resource models, we envision that FluxTrap's SIMD abstraction can serve as a hardware-software contract, paving the way for portable, modular, and architecture-aligned quantum compilation.

8 Acknowledgement

This work is supported in part by NSF 2048144, NSF 2422169, and NSF 2427109. Additional support was provided by NSF 2435382, Accelerating Fault-Tolerant Quantum Logic (FTL), and NSF 2016245, Quantum Leap Challenge Institute for Present and Future Quantum Computing (CIQC). This work was also supported by the U.S. Department of Energy, Office of Science, National Quantum Information Science Research Centers, Quantum Science Center (QSC). This research used resources of the Oak Ridge Leadership Computing Facility, a DOE Office of Science User Facility supported under Contract DE-AC05-00OR22725.

References

[1] Frank Arute, Kunal Arya, Ryan Babbush, Dave Bacon, Joseph C Bardin, Rami Barends, Rupak Biswas, Sergio Boixo, Fernando GSL Brandao, David A Buell, et al. Quantum supremacy using a programmable superconducting processor. *Nature*, 574(7779):505–510, 2019.

[2] He-Liang Huang, Dachao Wu, Daojin Fan, and Xiaobo Zhu. Superconducting quantum computing: a review. *Science China Information Sciences*, 63:1–32, 2020.

[3] Sergey Bravyi, Oliver Dial, Jay M Gambetta, Darío Gil, and Zaira Nazario. The future of quantum computing with superconducting qubits. *Journal of Applied Physics*, 132(16), 2022.

[4] Colin D Bruzewicz, John Chiaverini, Robert McConnell, and Jeremy M Sage. Trapped-ion quantum computing: Progress and challenges. *Applied Physics Reviews*, 6(2), 2019.

[5] Jwo-Sy Chen, Erik Nielsen, Matthew Ebert, Volkan Inlek, Kenneth Wright, Vandiver Chaplin, Andrii Maksymov, Eduardo Páez, Amrit Poudel, Peter Maunz, et al. Benchmarking a trapped-ion quantum computer with 29 algorithmic qubits. *arXiv preprint arXiv:2308.05071*, 2023.

[6] Pieter Kok, William J Munro, Kae Nemoto, Timothy C Ralph, Jonathan P Dowling, and Gerard J Milburn. Linear optical quantum computing with photonic qubits. *Reviews of modern physics*, 79(1):135–174, 2007.

[7] J Eli Bourassa, Rafael N Alexander, Michael Vasmer, Ashlesha Patil, Ilan Tzitrin, Takaya Matsuura, Daiqin Su, Ben Q Baragiola, Saikat Guha, Guillaume Dauphinais, et al. Blueprint for a scalable photonic fault-tolerant quantum computer. *Quantum*, 5:392, 2021.

[8] Dolev Bluvstein, Simon J Evered, Alexandra A Geim, Sophie H Li, Hengyun Zhou, Tom Manovitz, Sepehr Ebadi, Madelyn Cain, Marcin Kalinowski, Dominik Hangleiter, et al. Logical quantum processor based on reconfigurable atom arrays. *Nature*, 626(7997):58–65, 2024.

[9] Jonathan Wurtz, Alexei Bylinskii, Boris Braverman, Jesse Amato-Grill, Sergio H Cantu, Florian Huber, Alexander Lukin, Fangli Liu, Phillip Weinberg, John Long, et al. Aquila: Quera's 256-qubit neutral-atom quantum computer. *arXiv preprint arXiv:2306.11727*, 2023.

[10] Juan I Cirac and Peter Zoller. Quantum computations with cold trapped ions. *Physical review letters*, 74(20):4091, 1995.

[11] David Kielpinski, Chris Monroe, and David J Wineland. Architecture for a large-scale ion-trap quantum computer. *Nature*, 417(6890):709–711, 2002.

[12] Steven A Moses, Charles H Baldwin, Michael S Allman, R Ancona, L Ascarrunz, C Barnes, J Bartolotta, B Bjork, P Blanchard, M Bohn, et al. A race-track trapped-ion quantum processor. *Physical Review X*, 13(4):041052, 2023.

[13] Robert D Delaney, Lucas R Sletten, Matthew J Cich, Brian Estey, Maya I Fabrikant, David Hayes, Ian M Hoffman, James Hostetter, Christopher Langer, Steven A Moses, et al. Scalable multispecies ion transport in a grid-based surface-electrode trap. *Physical Review X*, 14(4):041028, 2024.

[14] M Akhtar, F Bonus, FR Lebrun-Gallagher, NI Johnson, M Siegele-Brown, S Hong, SJ Hile, SA Kulmiya, Sebastian Weidt, and WK Hensinger. A high-fidelity quantum matter-link between ion-trap microchip modules. *Nature communications*, 14(1):531, 2023.

[15] Colin D. Bruzewicz, John Chiaverini, Robert McConnell, and Jeremy M. Sage. Trapped-ion quantum computing: Progress and challenges. *Applied Physics Reviews*, 6(2), May 2019. URL: http://dx.doi.org/10.1063/1.5088164, doi:10.1063/1.5088164.

[16] M Malinowski, DTC Allcock, and CJ Ballance. How to wire a 1000-qubit trapped-ion quantum computer. *PRX Quantum*, 4(4):040313, 2023.

[17] Frank Arute, Kunal Arya, Ryan Babbush, Dave Bacon, Joseph C. Bardin, Rami Barends, Rupak Biswas, Sergio Boixo, Fernando G. S. L. Brandao, David A. Buell, Brian Burkett, Yu Chen, Zijun Chen, Ben Chiaro, Roberto Collins, William Courtney, Andrew Dunsworth, Edward Farhi, Brooks Foxen, Austin Fowler, Craig Gidney, Marissa Giustina, Rob Graff, Keith Guerin, Steve Habegger, Matthew P. Harrigan, Michael J. Hartmann, Alan Ho, Markus Hoffmann, Trent Huang, Travis S. Humble, Sergei V. Isakov, Evan Jeffrey, Zhang Jiang, Dvir Kafri, Kostyantyn Kechedzhi, Julian Kelly, Paul V. Klimov, Sergey Knysh, Alexander Korotkov, Fedor Kostritsa, David Landhuis, Mike Lindmark, Erik Lucero, Dmitry Lyakh, Salvatore Mandrà, Jarrod R. McClean, Matthew McEwen, Anthony Megrant, Xiao Mi, Kristel Michielsen, Masoud Mohseni, Josh Mutus, Ofer Naaman, Matthew Neeley, Charles Neill, Murphy Yuezhen Niu, Eric Ostby, Andre Petukhov, John C. Platt, Chris Quintana, Eleanor G. Rieffel, Pedram Roushan, Nicholas C. Rubin, Daniel Sank, Kevin J. Satzinger, Vadim Smelyanskiy, Kevin J. Sung, Matthew D. Trevithick, Amit Vainsencher, Benjamin Villalonga, Theodore White, Z. Jamie Yao, Ping Yeh, Adam Zalcman, Hartmut Neven, and John M. Martinis. Quantum supremacy using a programmable superconducting processor. *Nature*, 574(7779):505–510, October 2019. URL: http://dx.doi.org/10.1038/s41586-019-1666-5, doi:10.1038/s41586-019-1666-5.

[18] Abhinav Kandala, Antonio Mezzacapo, Kristan Temme, Maika Takita, Markus Brink, Jerry M. Chow, and Jay M. Gambetta. Hardware-efficient variational quantum eigensolver for small molecules and quantum magnets. *Nature*, 549(7671):242–246, September 2017. URL: http://dx.doi.org/10.1038/nature23879, doi:10.1038/nature23879.

[19] M Gutiérrez, M Müller, and Alejandro Bermúdez. Transversality and lattice surgery: Exploring realistic routes toward coupled logical qubits with trapped-ion quantum processors. *Physical Review A*, 99(2):022330, 2019.

[20] Ralph Duncan. A survey of parallel computer architectures. *Computer*, 23(2):5–16, 1990.

[21] Bao Bach, Ilya Safro, and Ed Younis. Efficient compilation for shuttling trapped-ion machines via the position graph architectural abstraction. *arXiv preprint arXiv:2501.12470*, 2025.

[22] Prakash Murali, Dripto M Debroy, Kenneth R Brown, and Margaret Martonosi. Architecting noisy intermediate-scale trapped ion quantum computers. In *2020 ACM/IEEE 47th Annual International Symposium on Computer Architecture (ISCA)*, pages 529–542. IEEE, 2020.

[23] Daniel Sanchez and Christos Kozyrakis. Zsim: Fast and accurate microarchitectural simulation of thousand-core systems. *ACM SIGARCH Computer architecture news*, 41(3):475–486, 2013.

[24] Juan M Pino, Jennifer M Dreiling, Caroline Figgatt, John P Gaebler, Steven A Moses, MS Allman, CH Baldwin, Michael Foss-Feig, David Hayes, Karl Mayer, et al. Demonstration of the trapped-ion quantum ccd computer architecture. *Nature*, 592(7853):209–213, 2021.

[25] K. Wright, K. M. Beck, S. Debnath, J. M. Amini, Y. Nam, N. Grzesiak, J.-S. Chen, N. C. Pisenti, M. Chmielewski, C. Collins, K. M. Hudek, J. Mizrahi, J. D. Wong-Campos, S. Allen, J. Apisdorf, P. Solomon, M. Williams, A. M. Ducore, A. Blinov, S. M. Kreikemeier, V. Chaplin, M. Keesan, C. Monroe, and J. Kim. Benchmarking an 11-qubit quantum computer. *Nature Communications*, 10(1), November 2019. URL: http://dx.doi.org/10.1038/s41467-019-13534-2, doi:10.1038/s41467-019-13534-2.

[26] Kenneth Wright, Jason M Amini, Daniel L Faircloth, Curtis Volin, S Charles Doret, Harley Hayden, C-S Pai, David W Landgren, Douglas Denison, Tyler Killian, Richart E Slusher, and Alexa W Harter. Reliable transport through a microfabricated x-junction surface-electrode ion trap. *New Journal of Physics*, 15(3):033004, mar 2013. URL: https://dx.doi.org/10.1088/1367-2630/15/3/033004, doi:10.1088/1367-2630/15/3/033004.

[27] Gushu Li, Yufei Ding, and Yuan Xie. Tackling the qubit mapping problem for nisq-era quantum devices, 2019. URL: https://arxiv.org/abs/1809.02573, arXiv:1809.02573.

[28] Qiskit contributors. Qiskit: An open-source framework for quantum computing, 2023. doi:10.5281/zenodo.2573505.

[29] Yukai Wu, Sheng-Tao Wang, and L.-M. Duan. Noise analysis for high-fidelity quantum entangling gates in an anharmonic linear paul trap. *Phys. Rev. A*, 97:062325, Jun 2018. URL: https://link.aps.org/doi/10.1103/PhysRevA.97.062325, doi:10.1103/PhysRevA.97.062325.

[30] Steven A Cuccaro, Thomas G Draper, Samuel A Kutin, and David Petrie Moulton. A new quantum ripple-carry addition circuit. *arXiv preprint quant-ph/0410184*, 2004. URL: https://arxiv.org/abs/quant-ph/0410184, doi:10.48550/arXiv.quant-ph/0410184.

[31] Max Alteg, Baptiste Chevalier, Octave Mestoudjian, and Johan-Luca Rossi. Study of adaptative derivative-assemble pseudo-trotter ansatzes in vqe through qiskit api. 2022. arXiv:2210.15438.

[32] Jia-Bin You, Dax Enshan Koh, Jian Feng Kong, Wen-Jun Ding, Ching Eng Png, and Lin Wu. Exploring variational quantum eigensolver ansatzes for the long-range xy model. 2021. arXiv:2109.00288.

[33] Teague Tomesh, Pranav Gokhale, Victory Omole, Gokul Subramanian Ravi, Kaitlin N Smith, Joshua Viszlai, Xin-Chuan Wu, Nikos Hardavellas, Margaret R Martonosi, and Frederic T Chong. Supermarq: A scalable quantum benchmark suite. In *2022 IEEE International Symposium on High-Performance Computer Architecture (HPCA)*, pages 587–603. IEEE, 2022.

[34] Ang Li, Samuel Stein, Sriram Krishnamoorthy, and James Ang. Qasmbench: A low-level quantum benchmark suite for nisq evaluation and simulation. *ACM Transactions on Quantum Computing*, 4(2):1–26, 2023.

[35] Austin G. Fowler, Matteo Mariantoni, John M. Martinis, and Andrew N. Cleland. Surface codes: Towards practical large-scale quantum computation. *Phys. Rev. A*, 86:032324, Sep 2012. URL: https://link.aps.org/doi/10.1103/PhysRevA.86.032324, doi:10.1103/PhysRevA.86.032324.

[36] Rajeev Acharya, Igor Aleiner, Richard Allen, Trond I. Andersen, Markus Ansmann, Frank Arute, Kunal Arya, Abraham Asfaw, Juan Atalaya, Ryan Babbush, Dave Bacon, Joseph C. Bardin, Joao Basso, Andreas Bengtsson, Sergio Boixo, Gina Bortoli, Alexandre Bourassa, Jenna Bovaird, Leon Brill, Michael Broughton, Bob B. Buckley, David A. Buell, Tim Burger, Brian Burkett, Nicholas Bushnell, Yu Chen, Zijun Chen, Ben Chiaro, Josh Cogan, Roberto Collins, Paul Conner, William Courtney, Alexander L. Crook, Ben Curtin, Dripto M. Debroy, Alexander Del Toro Barba, Sean Demura, Andrew Dunsworth, Daniel Eppens, Catherine Erickson, Lara Faoro, Edward Farhi, Reza Fatemi, Leslie Flores Burgos, Ebrahim Forati, Austin G. Fowler, Brooks Foxen, William Giang, Craig Gidney, Dar Gilboa, Marissa Giustina, Alejandro Grajales Dau, Jonathan A. Gross, Steve Habegger, Michael C. Hamilton, Matthew P. Harrigan, Sean D. Harrington, Oscar Higgott, Jeremy Hilton, Markus Hoffmann, Sabrina Hong, Trent Huang, Ashley Huff, William J. Huggins, Lev B. Ioffe, Sergei V. Isakov, Justin

Iveland, Evan Jeffrey, Zhang Jiang, Cody Jones, Pavol Juhas, Dvir Kafri, Kostyantyn Kechedzhi, Julian Kelly, Tanuj Khattar, Mostafa Khezri, Mária Kieferová, Seon Kim, Alexei Kitaev, Paul V. Klimov, Andrey R. Klots, Alexander N. Korotkov, Fedor Kostritsa, John Mark Kreikebaum, David Landhuis, Pavel Laptev, Kim-Ming Lau, Lily Laws, Joonho Lee, Kenny Lee, Brian J. Lester, Alexander Lill, Wayne Liu, Aditya Locharla, Erik Lucero, Fionn D. Malone, Jeffrey Marshall, Orion Martin, Jarrod R. McClean, Trevor Mccourt, Matt McEwen, Anthony Megrant, Bernardo Meurer Costa, Xiao Mi, Kevin C. Miao, Masoud Mohseni, Shirin Montazeri, Alexis Morvan, Emily Mount, Wojciech Mruczkiewicz, Ofer Naaman, Matthew Neeley, Charles Neill, Ani Nersisyan, Hartmut Neven, Michael Newman, Jiun How Ng, Anthony Nguyen, Murray Nguyen, Murphy Yuezhen Niu, Thomas E. O'Brien, Alex Opremcak, John Platt, Andre Petukhov, Rebecca Potter, Leonid P. Pryadko, Chris Quintana, Pedram Roushan, Nicholas C. Rubin, Negar Saei, Daniel Sank, Kannan Sankaragomathi, Kevin J. Satzinger, Henry F. Schurkus, Christopher Schuster, Michael J. Shearn, Aaron Shorter, Vladimir Shvarts, Jindra Skruzny, Vadim Smelyanskiy, W. Clarke Smith, George Sterling, Doug Strain, Marco Szalay, Alfredo Torres, Guifre Vidal, Benjamin Villalonga, Catherine Vollgraff Heidweiller, Theodore White, Cheng Xing, Z. Jamie Yao, Ping Yeh, Juhwan Yoo, Grayson Young, Adam Zalcman, Yaxing Zhang, and Ningfeng Zhu. Suppressing quantum errors by scaling a surface code logical qubit, 2022. URL: https://arxiv.org/abs/2207.06431, `arXiv:2207.06431`.

[37] John Preskill. Quantum computing in the nisq era and beyond. *Quantum*, 2:79, 2018.

[38] Ye Wang, Mark Um, Junhua Zhang, Shuoming An, Ming Lyu, Jing-Ning Zhang, L.-M. Duan, Dahyun Yum, and Kihwan Kim. Single-qubit quantum memory exceeding ten-minute coherence time. *Nature Photonics*, 11(10):646–650, September 2017. URL: http://dx.doi.org/10.1038/s41566-017-0007-1, `doi:10.1038/s41566-017-0007-1`.

[39] Sergey Bravyi and Alexei Kitaev. Universal quantum computation with ideal clifford gates and noisy ancillas. *Physical Review A—Atomic, Molecular, and Optical Physics*, 71(2):022316, 2005.

[40] Daniel Litinski. Magic state distillation: Not as costly as you think. *Quantum*, 3:205, 2019.

[41] Sergey Bravyi and Jeongwan Haah. Magic-state distillation with low overhead. *Physical Review A—Atomic, Molecular, and Optical Physics*, 86(5):052329, 2012.

[42] Tyler Leblond, Ryan S. Bennink, Justin G. Lietz, and Christopher M. Seck. Tiscc: A surface code compiler and resource estimator for trapped-ion processors. In *Proceedings of the SC '23 Workshops of the International Conference on High Performance Computing, Network, Storage, and Analysis*, SC-W 2023, page 1426–1435. ACM, November 2023. URL: http://dx.doi.org/10.1145/3624062.3624214, `doi:10.1145/3624062.3624214`.

[43] Craig Gidney. Stim: a fast stabilizer circuit simulator. *Quantum*, 5:497, July 2021. URL: http://dx.doi.org/10.22331/q-2021-07-06-497, `doi:10.22331/q-2021-07-06-497`.

[44] Oscar Higgott. Pymatching: A python package for decoding quantum codes with minimum-weight perfect matching. *ACM Transactions on Quantum Computing*, 3(3):1–16, 2022.